Langmuir

Article

pubs.acs.org/Langmuir

Utilization of Cavity Vortex To Delay the Wetting Transition in One-Dimensional Structured Microchannels

Anvesh Gaddam,[†] Amit Agrawal,[*,†] Suhas S. Joshi,[†] and M. C. Thompson[‡]

[†]Department of Mechanical Engineering, Indian Institute of Technology Bombay, Powai, Mumbai 400076, India

[‡]Fluids Laboratory for Aeronautical and Industrial Research (FLAIR), Department of Mechanical and Aerospace Engineering, Monash University, Clayton 3800, Australia

ABSTRACT: Frictional resistance across rough surfaces depends on the existence of slip on the liquid−gas interface; therefore, prolonging the existence of liquid−gas interface becomes relevant. In this work, we explore manipulation of the cavity shape in order to delay the wetting transition. We propose that liquid-driven vortices generated in the air cavity dissipate sufficient energy to delay the Cassie−Wenzel transition. Toward this, we fabricated cavities on the side walls of a polydimethylsiloxane-based microchannel for easy visualization and analysis of the dynamics of the liquid−gas interface. Two distinct flow regimes are identified in the experimental envelope. In the first regime, the liquid−gas interface is found to be protruding into the flow field, thus increasing the pressure drop at low Reynolds number. In the second regime, flow rate and geometry-based wetting transitions are established at moderate to high Reynolds numbers. We then investigate the effect of different cavity shapes (square, trapezoidal, and U-shape) in delaying the wetting transition by manipulating liquid-driven vortices. Out of the shapes considered in this study, trapezoidal cavities perform better than cavities with vertical walls in delaying the wetting transition due to geometrical squeezing of vortices toward the liquid−gas interface. Numerical simulations corroborate the experimental findings in that cavities with inclined walls exert more force on the liquid−gas interface, thus delaying their wetting transition. The proposed method being passive in nature appears more attractive than previous active methods.

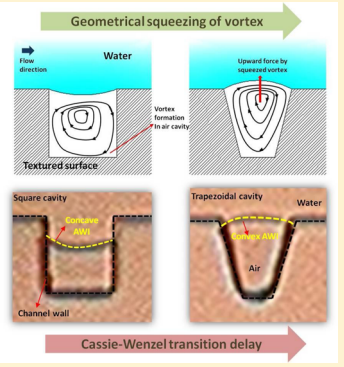

1. INTRODUCTION

Transportation and handling of liquids at microscale have led to the development of innovative products and solutions in application areas such as chemical, biotechnology, and medical diagnostics. Bulk fluid sample metering is ubiquitous in many capillary-driven immunoassays and pressure-driven microfluidic large-scale integration platforms.[1] Despite its success, liquid handling in miniaturized systems faces a fundamental challenge as the pumping power required to transport liquids across microchannels rapidly increases with a decrease in the characteristic length scale of the system: $\Delta P \sim 1/l^4$, where ΔP is the pressure drop across the microchannel and l is the characteristic length scale of the system.[2] This severe resistance to liquid flow at the microscale is promoted by large surface area to volume ratio. Manipulation of surface wettability has the ability to play a crucial role in enhancing transportation of small liquid volumes through microchannels, together with alternate actuation mechanisms for driving the flow (electrowetting,[3] magnetofluidics,[4] and capillary filling[5]). Although tailoring of wettability through chemical modification of surfaces has been explored in the past, an alternative of altering the topography of the surfaces (configuration, roughness, or texture) offers substantial benefits, possibly without affecting the biocompatibility of the surface material.[6,7]

Surface roughness at micro and nano scales allows a liquid−solid interface to exist in two different states, namely, the Cassie−Baxter state (CBS) and the Wenzel state (WS). In the former, gas is trapped inside surface cavities and the liquid is pinned at the asperities, resulting in a heterogeneous interface. In contrast, when in the latter state, liquid fills the cavities forming a homogeneous liquid−solid interface. The existence of the CBS or WS depends on parameters such as the scale of roughness,[8] surface chemistry, and even the history of the surface.[9] In general, CBS offers higher contact angle and lower hysteresis in contact angle than WS; thereby, a rough surface behaves as a hydrophobic surface in the CBS. Selective roughening of microfluidic platforms has therefore been suggested for droplet manipulation,[10] bulk liquid transport,[11] and microparticle fractionation.[12] The CBS decreases the effective liquid−solid contact area because of the air-filled cavities, thereby reducing the wall shear stress. Thus, the CBS unwraps a plethora of benefits through energy savings. However, in practical operating conditions, CBS is metastable, and external stimuli such as gravity,[13] vibration,[14] hydraulic pressure,[9] or kinetic energy[15] can trigger the transition to highly stable WS. The energy barrier between the Cassie−Baxter and Wenzel states is estimated to be of the order of 10^{-9} J for a droplet sitting on a rough substrate.[16] The CBS−WS energy barrier is also shown to increase with the contribution from depinning of the three-phase contact line.[17]

Received: October 3, 2015
Revised: November 21, 2015
Published: November 24, 2015

DOI: 10.1021/acs.langmuir.5b03666
Langmuir 2015, 31, 13373−13384

Few researchers carried out experiments in static conditions to examine the wetting transitions. Bobji et al.[18] experimentally visualized wetting transitions in both random and structured roughness on surfaces by employing a total internal reflection technique. Poetes et al.[19] conducted experiments under water for Teflon-coated rough surfaces and observed that the lifetime of the plastron (gas layer) decreases exponentially with an increase in immersion depth. They attributed the diffusion of gas from the cavities into the surrounding liquid as the driving mechanism responsible for wetting of the cavities. A similar observation, using an optical characterization method, was reported by Samaha et al.[20] Their experiments suggested that using a fibrous coating improves the longevity of the superhydrophobic surface in comparison with the rough surface. Hence, it is concluded that gas diffusion plays an important role in the CBS−WS transition under static conditions.

Since retention of the Cassie state appears to be crucial for ensuring that surfaces remain hydrophobic, a variety of active and passive methods have been explored. Application of external energy such as an electric field,[21] vibration,[14] and regulation of pressure[22] to delay the transition has been studied. Since active control methods require additional expenditure of energy, passive methods of delaying or avoiding the CBS−WS transition are of much interest. In passive methods, increasing the height of textures,[23,24] adding secondary textures on top of primary textures,[26] varying the shape of textures,[23] and their spacing[25] were reported to delay the CBS−WS transition. Hensel et al.[27] reported that the pressure required to induce a transition from CBS to WS is increased by protrusions on the walls of the cavities. The profile of such protrusions was found to play a role in the transition. They showed that the transition could be made reversible by tuning the pressure above the cavities. Our literature survey shows that a large body of work has been undertaken for predicting and quantifying transition with respect to topological parameters but is restricted to *static* conditions. The interest of the current work is in delaying the CBS−WS transition in *flow* conditions which is relevant in applications ranging from microfluidics to underwater vehicles.[28]

In the case of bulk liquid transport across textured surfaces, momentum transfer across the liquid−gas interface is expected to a have significant impact on the CBS−WS transition in conjunction with other factors mentioned earlier. In closed systems, channel confinement also affects the transition dynamics even at low Reynolds number.[29] In contrast to densely packed structures, which resist wetting transition in static conditions, a surface with sparsely spaced structures offers lower frictional resistance in bulk fluid transport on hydrophobic surfaces. The maximum velocity of liquid without suffering wetting transition was found to be a function of texture spacing even in transport of liquid droplets.[30] Thus, the optimal design of textured surfaces has to be a compromise between these two design criteria: increasing the volume flow rate through a microchannel and avoiding the wetting transition. Lauga and Stone[8] compared the effectiveness of various textures by calculating the slip length (an imaginary distance below the liquid−gas interface where no-slip condition is recovered) in pressure-driven flows. Since the slip length has a logarithmic dependence on spacing between the structures, widely spaced structures experience a lower pressure drop. Widely spaced structures are however obviously more prone to the CBS−WS transition though a gain in slippage is possible.[31] It is therefore essential to develop strategies to avoid the CBS−WS transition in widely spaced structures in order to achieve maximum slip length on textured surfaces. Lee and Kim[32] introduced nanostructures on posts; these act as pinning sites to the propagating meniscus, thereby delaying the wetting transition. Self-regulating designs have also been proposed to avoid the wetting transition.[33] The above strategies are based on the principle of increasing the energy barrier required for the CBS−WS transition.

In the present work, we utilize a passive control strategy involving variation in the cavity shape and demonstrate that the CBS−WS transition can be delayed. Our hypothesis is that the location and strength of the vortex trapped in the air cavity play a significant role in affecting this transition. In order to verify this hypothesis, air cavities of different shapes such as rectangular, trapezoidal, and U-type were experimentally and numerically studied at different flow rates. In all the cases, the gas fraction was kept constant at 50% for comparison of performance as a function of cavity shape and size. We also comment on the friction reduction behavior and argue that certain aspects could be different for static and flow conditions. We recognize that understanding the wetting transition is challenging at microscale because of difficulty in visualizing the liquid−gas interface; here, this issue was overcome by employing cavities on the side walls of the microchannel.

2. THEORY

In general, the hydraulic pressure is equally distributed on flat surfaces in a static fluid. If the surface is decorated with cavities with the same gas fraction, the liquid−gas meniscus should ideally have the same curvature over every gas cavity under static conditions, as shown in Figure 1a. The local liquid pressure above the gas cavity drives the liquid−gas interface into the cavity, while surface tension (γ) of the interface and gas pressure (P) resist this action. The critical pressure required to prevent the collapse of the liquid−gas meniscus is given by the Young−Laplace equation. If the pressure difference across the liquid−gas interface ($P_{water} - P_{air}$) exceeds the capillary pressure ($P_{Laplace}$), the surface tension can no longer sustain the weight of liquid column, leading to a collapse.

The CBS−WS transition occurs through three stages under static conditions.[34] In the first stage, an increase in hydraulic pressure of the liquid causes the liquid−gas interface to deform into the gas cavities with the interface remaining pinned at the edges of the cavity. This in turn reduces the gas cavity volume and thereby increases the cavity gas pressure. The pressure difference across the liquid−gas interface gradually reduces due to the increase in gas pressure in the cavity. In the second stage, with an increase in pressure above the gas cavity, the interface depins and slides along the walls of the cavity for high-aspect-ratio structures. In the final stage, the sagged liquid−gas interface touches the bottom of the gas cavity, thus completing the transition to WS. For shorter structures, the sequence of transitions is different. Here, the transition occurs even if the interface remains pinned at the edges while the deformed liquid−gas interface touches the bottom of the cavity (Figure 1a, inset). Confocal microscopy-based visualization[35] of liquid−gas menisci reveal that the transition sequence indeed follows the three stages explained above under static conditions. However, it is shown that another stable intermediate state also exists in certain conditions where the side wall is inclined.[36] In this state, the liquid−gas interface touches the bottom surface

DOI: 10.1021/acs.langmuir.5b03666
Langmuir 2015, 31, 13373−13384

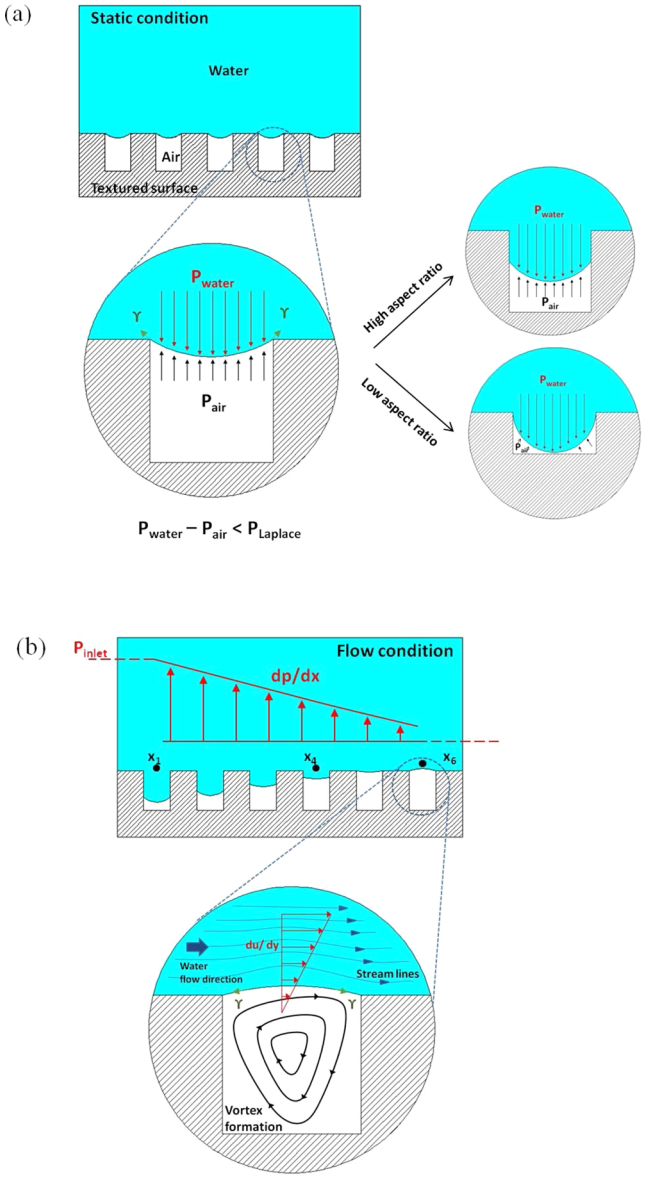

Figure 1. (a) Wetting transition at static conditions. (b) Dynamics of liquid–gas interface during flow condition.

and the CBS can be retained by lowering the pressure of the liquid.

In confined flows, a pressure gradient (dp/dx) is required to drive the liquid through the passage. Since the local pressure in the microchannel decreases monotonically with streamwise location, the force driving the liquid–gas interface also changes with streamwise position (see Figure 1b). A larger penetration of liquid–gas interface into the cavity is expected at the inlet cavity due to a relatively larger local pressure difference ($p[x_1] - p_{air}$). Since the local pressure difference at a cavity situated at the midsection ($p[x_4] - p_{air}$) is less than that at the inlet ($p[x_1] - p_{air}$), only minor penetration is expected at the middle location. Note that in certain cases ($p_{air} > p[x_6]$); the liquid–gas interface may become convex. This convex interface may in turn displace the streamlines in the core liquid flow region (see Figure 1b, inset). The movement of streamlines toward/away from the wall of the microchannel implies that the flow experiences local deceleration/acceleration. This local acceleration/deceleration of the flow can increase the overall pressure drop across the microchannel.

The transfer of momentum (du/dy) of the flowing liquid into the cavity across the interface is also represented schematically in Figure 1b. Unlike static conditions, liquid sliding across the gas column generates a circulation cell inside the cavity. This situation is analogous to a lid-driven cavity flow. The vortex generated inside the cavity (Figure 1b, inset) carries circulation, which depends on the flow velocity, cavity shape and size, and fluid properties. The circulating vortex leads to dissipation of energy and can therefore be considered as an additional resistive force on the liquid–gas interface. The transfer of momentum across the interface therefore serves as an additional factor affecting the CBS–WS transition. The size, strength, and location of a cavity vortex can be manipulated by appropriate design of the cavity shape. We therefore recognize that if manipulated properly, the cavity vortex may exert sufficient force to delay the premature CBS–WS transition.

3. METHODOLOGY

In order to visualize the dynamics of a liquid–gas interface and characterize the frictional effects of cavities in both Cassie and Wenzel states, a series of experiments have been performed at different flow rates. In addition, numerical modeling was adopted to understand the effect of the vortex dynamics within the air cavity on the liquid–gas interface.

3.1. Fabrication and Flow Experimentation. A schematic of the experimental setup, also showing the dimensions of microchannels, is provided in Figure 2. The

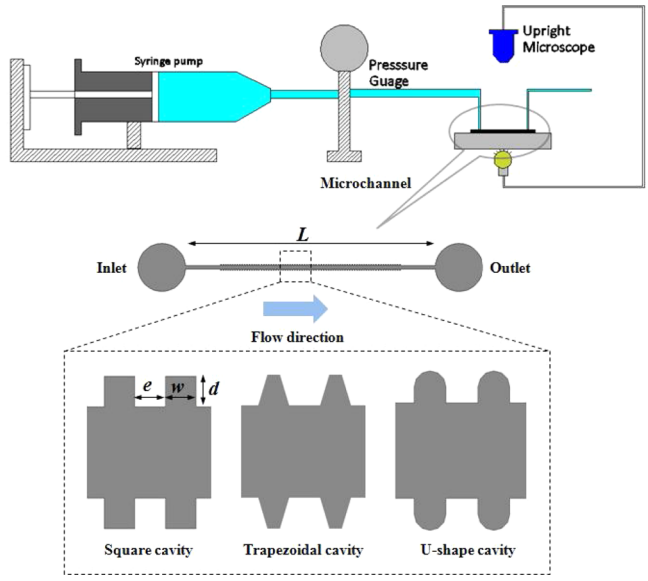

Figure 2. Schematic of experimental setup and microchannel with cavities of various shapes is shown. The dark region in the inset corresponds to the region of fluid flow.

height (h) of the microchannel is 100 μm, width (b) is 300 μm, and length (L) is 26 mm. The length of the microchannel is chosen to avoid blockage effect (see below) and also based on constraints in fabrication (such as the edge bead effect[37]). The distance between the cavities (e) is 100 μm, and their depth (d) is maintained at 100 μm. The top width (w) of cavity is kept at 100 μm. A total of 100 cavities were decorated along the side wall of the microchannel as shown in Figure 2, which shows an enlarged view of the microchannel with given specifications.

DOI: 10.1021/acs.langmuir.5b03666
Langmuir 2015, 31, 13373–13384

Four different types of cavities are considered in this study. To quantify the effect of the size of the cavities on air entrapment and friction reduction, the number of cavities inside the microchannel is increased while keeping the gas fraction constant (50%). Here, the gas fraction ($\delta = e/(e + w)$) is defined as ratio of projected area of air pockets to the total area of the channel considering only the inner diameter. This give rise to two cases: square cavities and narrow rectangular cavities. In order to verify cavity vortex-based transition delay, trapezoidal and U-shaped cavities are also fabricated (see Figure 2).

Photolithography was used to fabricate a mold of microchannels with side cavities on silicon wafers. An oxidized silicon wafer was spin-coated with SU8-2100 negative photoresist to achieve the required height of the microchannel. Then standard photolithography was carried out to process the final mold. A PDMS base and curing agent (Sylgard 184, Dow Corning, USA) were mixed in the ratio of 10:1 and poured in the mold. Simultaneously, the PDMS base and curing agent were mixed in a 20:1 ratio and poured on a flat glass plate. Both the slabs are baked for 30 min at 65 °C. After becoming sufficiently hard, the patterned PDMS slab was peeled off from the mold, and 2 mm holes were punched for accommodating inlet and outlet ports on the slab. Then, the uncured plain PDMS slab and patterned PDMS slab were bonded to each other and baked overnight at 95 °C for cross-linking of the polymer to take place.

A flow rate of deionized water 0.06 and 0.3 mL/min was fed through the inlet of the microchannel using a syringe pump (Cole-Parmer), while the outlet was kept open to the atmosphere. A pressure transducer (Keller, UK) was connected between the syringe pump and inlet of the microchannel to record the pressure drop across the microchannel and the external tubing. Losses from external tubing were deducted from final pressure drop readings. Each measurement was carried out for 10 min to visualize the air–water interface dynamics. The total pressure drop is averaged over a 10 min period to quantify frictional effects due to wetting of the cavities. A constant temperature was maintained ensuring that there was no variation in viscosity during the measurements. An upright microscope was used to visualize the air–water interface. The dynamics of the air–water interface was recorded using a CCD camera attached to the microscope at an interval of 1 min between measurements. Movement of the air–water interface inside the cavities is measured with the aid of image-processing software (ImageJ).

3.2. Numerical Simulation of Liquid-Driven Vortices. The Navier–Stokes equations are solved using a finite-volume approach in two coupled domains in order to simulate water flow past cavities filled with air. A commercial CFD package ANSYS-Fluent is used to perform the simulations. In most of the numerical works, the liquid–gas interface is assumed to be shear-free to simplify the modeling. This assumption is based on negligible shear stress exerted by the air on the liquid flowing over the cavity. However, Davies et al.[38] showed that resistance across a liquid–gas interface leads to a significantly reduced slip length compared with predictions based on the shear-free (or infinite slip-length) assumption. In general, the shear-free assumption nullifies the effect of the underlying physical mechanisms operating in the cavities and at the interface.

Since vortices are generated within each air cavity due to the flowing liquid above, it is imperative to consider the coupling of the air and water domains in order to understand the dynamics of air flow in the cavities. In this study, four different geometries of cavities are chosen: square, trapezoidal, triangular, and U-shaped. For the numerical modeling, a unit module containing a single cavity is considered, and appropriate boundary conditions are applied, as shown in Figure 3. To understand

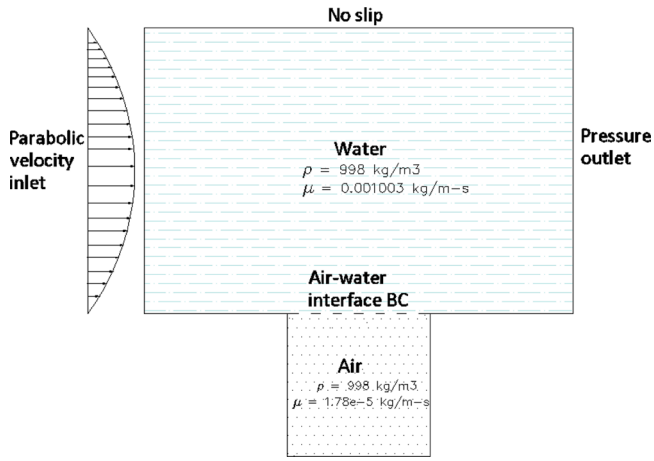

Figure 3. Computational domain consisting of one cavity with boundary conditions shown.

the behavior of the vortical flow, a coupled boundary condition is applied at the air–water interface that matches the shear stress and velocities across the interface. A user-defined function is employed to impose this boundary condition at the air–water interface. As ANSYS-Fluent allows prescribing either shear stress or velocity at an interface, a velocity condition is applied at the water zone interface and a shear stress condition applied at the air zone interface. For convenience, and as a first approximation, the air–water interface is assumed to be flat. At the inlet, an equilibrium parabolic velocity profile is imposed and pressure is set to be atmospheric at the outlet. A structured Cartesian mesh is generated using Gambit meshing software available in the ANSYS suite.

3.3. Data Reduction. The flow is nondimensionalized based on Reynolds number. Here, Reynolds number is given by $\mathrm{Re} = \rho u_{in} D_H/\mu_w$, where ρ is density of the water, u_{in} is the velocity at the inlet, D_H is the hydraulic diameter of the channel, and μ_w is the dynamic viscosity of water. The pressure drop measurements then were converted into the Poiseuille number, Po, which is a product of the Fanning friction factor and Reynolds number (f·Re) appropriate for laminar duct flows giving

$$\mathrm{Po} = \frac{2\Delta P D_H^{\,2}}{u_{in}\mu_w L} \tag{1}$$

where ΔP is the pressure drop between inlet and outlet, L is length of the microchannel, and other the variables have been introduced above.

4. RESULTS

The four factors relevant for determining the liquid–gas interface position are the pressure difference across the interface, surface tension, characteristics of surface, and cavity vortex. Based on these factors, the wetting characteristics can be categorized into three different cases: static, low Re (section

DOI: 10.1021/acs.langmuir.5b03666
Langmuir 2015, 31, 13373–13384

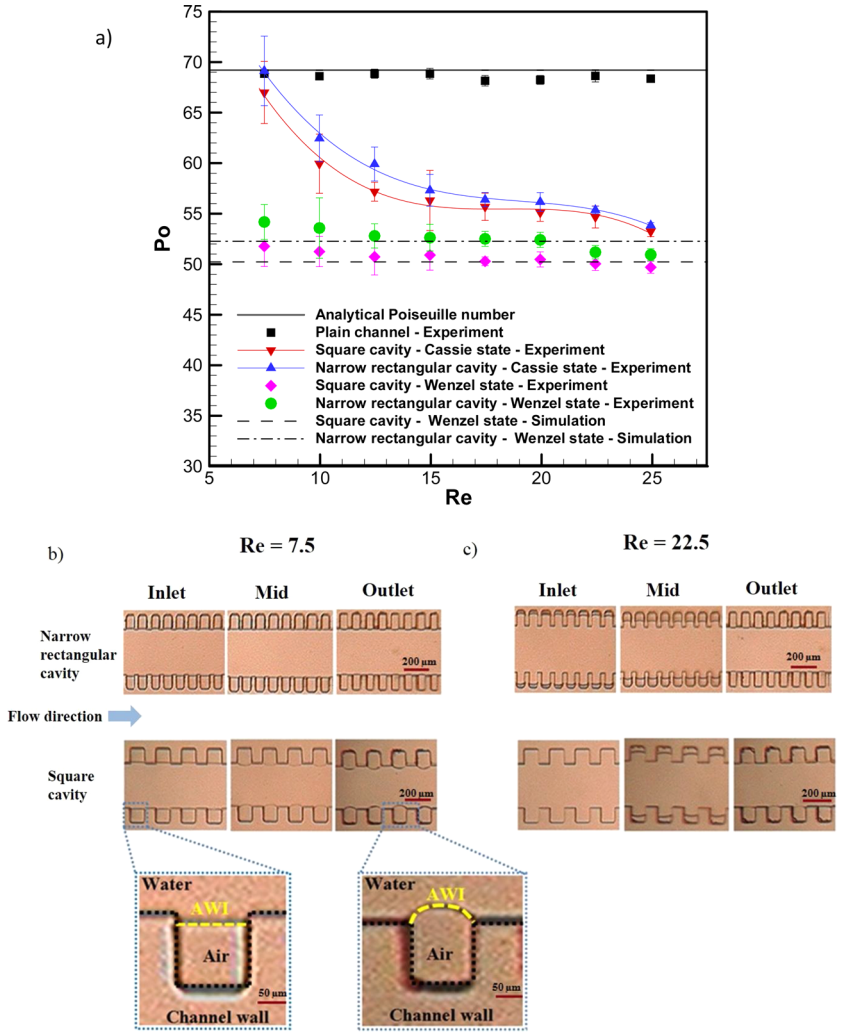

Figure 4. (a) Variation of Poiseuille number with Reynolds number for cavities in either Cassie or Wenzel states for channels with square or narrow rectangular cavities. Wetting transition for square and narrow rectangular cavities: (b) medium flow rate (Re = 7.5); (c) high flow rates (Re = 22.5) (AWI: air−water interface).

4.2), and high Re (section 4.1). The distinction between the last two regimes is based on pressure drop measurements and liquid−gas interface location.

4.1. Pressure Drop Characteristics for the Moderate/High Reynolds Number Regime (7.5 ≤ Re ≤ 25). For this set of experiments, the pressure drop measurements are carried out at *moderate to high* flow rates between 0.09 and 0.3 mL/min in a plain microchannel without cavities and for a channel with rectangular cavities. Figure 4a shows that the pressure drop (nondimensionalized to Poiseuille number) versus flow rate (nondimensionalized to Reynolds number) across a plain microchannel agrees well with the theoretical value. This good initial agreement helps to validate further measurements. It is further observed from the figure that Po for a microchannel with cavities is smaller than for the plain microchannel case. In fact, the figure suggests that two states of the flow are possible in a microchannel with cavities: in the first case, Po attains a constant value corresponding to a flow in the Wenzel state; while in the second case, the Poiseuille number value is a function of Reynolds number, corresponding to a flow in the Cassie−Baxter state.

For a fully wetted (Wenzel) state, a microchannel with cavities is pressurized (by the high-speed flowing water) until all the air pockets within the cavities disappear completely. Subsequently, the flow rate is reduced, corresponding to 7.5 ≤ Re ≤ 25, and the resultant value of the pressure drop at steady state is recorded. Figure 4a shows that for both square and narrow rectangular cavities, Po is smaller than that for a plain microchannel. The reason for this observation is discussed in section 6. Figure 4a also includes the value of Po obtained from three-dimensional numerical simulations of flow through the microchannel with the square and narrow rectangular cavities in the Wenzel state, for the purpose of comparison. Although a slight decrease (3.9% for square cavity and 5.9% for narrow cavities) in the value of Po is observed in the experiments for the Wenzel state, it can be noted from Figure 4a that the variation in Po falls within the uncertainty limits of the measurements. Furthermore, the figure also shows that narrow rectangular cavities have higher Po value (or pressure drop) compared to square cavities. This is attributed to the movement of streamlines into/out from cavities as the flow occurs. The overall number of cavities is larger for the microchannel having narrow rectangular cavities compared to the microchannel having square cavities. The movement of streamlines into/out from the cavities, and the corresponding local deceleration/acceleration of the flow, are therefore both increased for narrow

DOI: 10.1021/acs.langmuir.5b03666
Langmuir 2015, 31, 13373−13384

rectangular cavities. This leads to a larger pressure drop in the microchannel having narrow rectangular cavities.

In order to understand the dependence of Po on Re seen in Figure 4a for flow in the Cassie state, flow visualization experiments were also conducted. The flow visualization experiments were performed concurrently with the pressure measurements. The position of air−water interface at three locations of the microchannel (inlet, midposition, and outlet) after 10 min is shown in Figures 4b,c. Note that the measurements at these three locations have been conducted by moving the viewing zone from one position to another in a single experiment. The images therefore correspond to identical flow conditions. The images are shown for two different Reynolds numbers (moderate: Re = 7.5; high: Re = 22.5). At Re = 7.5, air is retained in the cavities at all the three locations, as evident from the air−water interface position, which is approximately in line with the inner width of the microchannel (Figure 4b). On the other hand, at Re = 22.5, water has fully penetrated the inlet cavities (Figure 4c). The penetration of water into the cavities is incomplete at the midlocation, while there is no penetration at the outlet cavities. Depression of the air−water interface inside the cavity at the inlet of the microchannel is observed due a relatively higher driving pressure at the inlet, as explained in section 2. In a similar vein, protrusion of the air−water interface into the microchannel at the outlet is observed in Figure 4a due to reduction in local pressure. In fact, the existence of a streamwise pressure gradient should cause a monotonic decrease in the local pressure difference across the liquid−gas interface along the length of the microchannel (Figure 1b).

In order to capture the interplay between the local pressure difference across the interface and the surface tension, a separate set of flow visualization experiments was conducted. Figure 5 shows an image for a channel with narrow rectangular

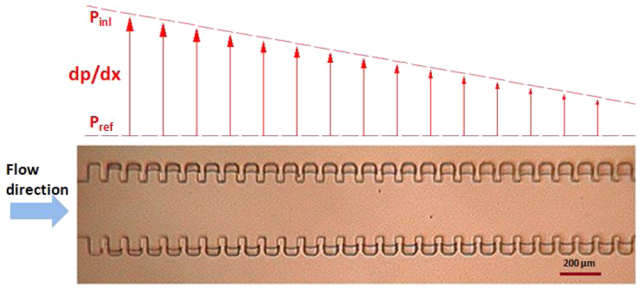

Figure 5. Experimental image showing variation in air−water interface along the length of a microchannel with narrow rectangular cavities at Re = 15. The view frame covers 15% of the total length of the microchannel.

cavities at Re = 15. The figure indeed depicts a smooth variation of the air−water interface inside the cavities. The smoothness in the variation of height of the air cavity lends weight to the quality of the present experimental results. A similar variation in the interface location has been suggested by a theoretical analysis in a slightly different context (i.e., the entry region of a microchannel) by Chakraborty and Anand.[39] The present observation supports the conjecture that the streamwise pressure gradient causes variation in the position of the liquid−gas interface along the length of the microchannel. As the capillary pressure (which is a function of the size of the cavity) remains constant, the surface tension forces and local pressure difference across the interface govern the position of the interface throughout the microchannel. As an aside, we remark that these air cavities could even be utilized as local pressure measurement sensors.

As shown in Figure 4a, the Po for a microchannel with cavities reduces with Re; the Po for flow in a smooth microchannel and Po for flow in a fully wetted (Wenzel) microchannel act as the two limits. From the flow visualization, it therefore becomes apparent that the dependence of Po on Re noted in the figure is because the flow is in the Cassie−Baxter state. Figure 4b shows that the air−water interface is protruding into the flow stream at the middle and outlet sections of the microchannel. This protrusion of the air−water interface leads to a reduction in the effective width of the microchannel, leading to higher value of Po at low Re. A detailed analysis of constriction effects caused by protruding menisci will be discussed in the next section.

As the flow rate is increased across the microchannel, the local pressure difference across the liquid−gas interface overcomes the capillary pressure of the cavity. This leads to depinning of the liquid−gas meniscus at the edges of the cavity and gradual descending of the meniscus occurs inside the cavity (Figure 4c). The sliding meniscus causes a change in the effective flow width of the microchannel. The increase in effective flow width leads to reduced flow friction in the microchannel; thereby, lower relative Po is observed at high flow rates. This effect becomes exaggerated in the case of narrow rectangular cavities, where the capillary pressure of a given cavity is increased compared to a square cavity due to the smaller size of the opening. The increase in capillary pressure offers higher resistance to the progressing liquid−gas meniscus inside narrow rectangular cavities. This resistance aids in maintaining air pockets in narrow rectangular cavities; the water flow rate therefore corresponds to a smaller microchannel width. Hence, a higher value of Po is observed for a microchannel having narrow rectangular cavities as compared to one with square cavities.

4.2. Pressure Drop Characteristics at Low Reynolds Number Regime (Re ≤ 5). Flow experiments were also carried out in the low Reynolds number regime where decreased hydraulic pressure is exerted on the air−water interface above the cavities. The relatively small flow rate corresponds to a lower pressure drop in the microchannel, and therefore a smaller pressure difference exists across the air−water interface. For these experiments, the pressure drop across the microchannel is recorded for a 10 min period concurrently with a visualization study of the air−water interface over that time.

Figure 6 shows the variation of pressure drop for square cavities over a period of 10 min; the pressure drop is found to increase linearly with time. It is interesting to note that the pressure drop is higher at low flow rates compared to a plain microchannel, despite the flow being in the Cassie−Baxter state. The reason for this is that the air−water interface expands into a *convex* shape and protrudes into the main flow (Figure 6c), thereby obstructing the flow. The protrusion of the interface varies gradually along the length of the microchannel; it is more at the outlet followed by mid- and inlet sections. This expansion of the interface into the main flow reduces the effective width of the microchannel for streamwise flow in contrast to the enhancement of the effective flow area observed at higher flow rates. Notice that there is a growth in cavity-air volume with time, as shown in Figure 6c. The form (convex or concave) and size of the liquid−gas interface are a function of

DOI: 10.1021/acs.langmuir.5b03666
Langmuir 2015, 31, 13373−13384

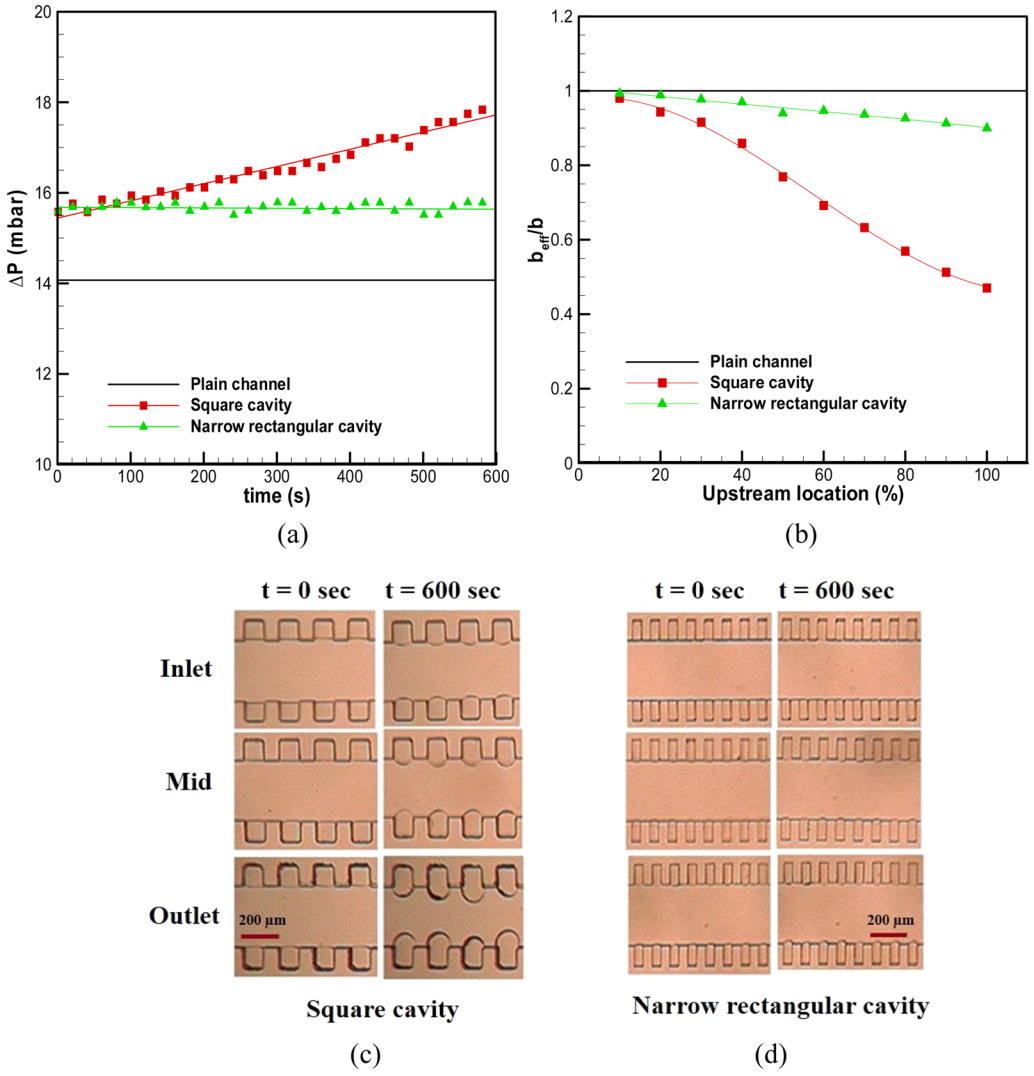

Figure 6. (a) Variation of pressure drop with time for square and narrow rectangular cavities. (b) Effective flow width of the channel along the length of the cavity. (c) Images showing air–water menisci at two time instants for square cavities. (d) Images showing air–water meniscus at two time instants for narrow rectangular cavities.

the surface tension, pressure difference across the interface, and vortical flow inside the cavity (introduced in section 2 and discussed further in section 5). At low flow rates, the pressure difference across the air–water interface and strength of vortex are not dominant; the growth of the air–water interface is therefore attributed to the hydrophobic nature of the surface. Here, the edge of cavity acts as pinning site for the liquid–gas interface, while the interface evolves with time to a strongly convex shape.

In order to understand the hydrophobicity effect on the interface shape, another set of experiments was carried out on narrow rectangular cavities under similar flow conditions. It was observed from Figure 6d that the growth of the interface with time for narrow rectangular cavities was not as high compared to square cavities. The competition between surface tension at the air–water interface, pressure acting above the cavities, and shear-driven vortices determines the penetration of the convex interface into the flow field. Since the surface tension forces are higher in small size cavities (narrow rectangular cavity) as compared to large size cavities (square cavity), the resistance to deformation of the air–water interface is more in the case of narrow rectangular cavities. Therefore, the temporal evolution of convex shaped air–water interface was observed to a lesser extent in narrow rectangular cavities of Figure 6d. With both square and rectangular cavities, depinning of the liquid–gas meniscus is observed after about 10 min (not shown). The depinning is followed by merging of adjoining (convex) interfaces.

In order to quantify the variation of the effective flow width with position, the displacement of the air–water interface into the main flow at various streamwise locations is calculated. The distance between the peak positions of the convex interface is measured using image-processing software. The data are averaged over ten cavities and normalized with the channel inner width, at ten different locations along the length of the microchannel. From Figure 6b it is apparent that the penetration of the air–water interface into the main flow is drastic in the case of square cavities compared to narrow rectangular cavities. In the case of a microchannel with square cavities, constriction of the flow width amounted to up to 50% of the inner width at the outlet compared to a maximum of 10% of the inner width for narrow rectangular cavities. As the streamwise variation in the effective flow width is negligible for the microchannel with narrow rectangular cavities, the pressure

DOI: 10.1021/acs.langmuir.5b03666
Langmuir 2015, 31, 13373–13384

drop remains same over the duration of the experiment (10 min) as shown in Figure 6a.

In this section, we have demonstrated that the pressure drop within a textured microchannel is greater than for a plain microchannel for low Reynolds numbers. The interface is also convex in shape as opposed to mostly concave for higher Reynolds numbers. These differences led to classifying the flow state into two different (moderate/high Re and low Re) flow regimes.

5. EFFECT OF CAVITY SHAPE ON THE AIR–WATER INTERFACE

As discussed in section 2, water flowing over cavities generates bulk vortical flow inside the air cavity, analogous to lid-driven cavity flow. The formation of vortices can result in a finite force on the air–water interface and can therefore affect the movement of the interface. These vortices dissipate energy inside the cavities; therefore, manipulation of these vortices could bring beneficial consequences in delaying the CBS–WS transition. In this section, we present experimental and numerical results pertaining to the manipulation of these vortices by changing the cavity shape.

To test the above hypothesis, numerical simulations were first carried out to visualize and quantify the vortex dynamics inside air cavities. All the simulations are carried out at Re = 1. Figure 7a (inset) depicts streamlines highlighting the vortical flow in an air cavity for the different shapes (square, U, trapezoidal, triangular) considered in the study. It is observed that the location of the vortex and its shape change with the geometry of the cavity. It is evident that the center of the vortex for both triangular and trapezoidal cavities is closer to the air–water interface compared to that for square and U-shaped cavities. That is the inclination of the side walls seems to squeeze the vortex pushing it toward the air–water interface. Zhang et al.[40] also showed similar movement of vortices with inclination of side wall in lid-driven cavity flows using lattice-Boltzmann-based simulations. Figure 7a also shows the variation of the flow velocity with the depth of the cavity for all considered geometries. Here, the location of the center of a vortex corresponds to kink in the velocity profile. These velocity profiles support the streamline plots discussed above.

The above numerical results were verified experimentally by fabricating microchannels with different cavity geometries. Three cavity geometries were chosen for the experiments: square, trapezoidal, and U-shaped. (Triangular cavity was not included because of difficulty in their fabrication.) Flow rates are varied corresponding to $7.5 < Re < 25$, and pressure drop measurements are converted to Po. Variation of Po with Re for all cavity geometries is shown in Figure 7b. The value of Po for trapezoidal cavities is more than both square and U-shaped cavities. The reason for this behavior is that the flow width is larger for square and U-shaped cavities, as demonstrated later through Figure 8. It is also interesting to note that Po from square and U-shaped cavities are approximately the same. This observation therefore supports the numerical prediction that the center of the vortex is at almost the same location for these cavity shapes.

Flow visualization experiments were additionally carried out to further confirm the above behaviors. Figure 8 presents images taken at the inlet, mid, and outlet of microchannels with square, U-shaped, and trapezoidal cavities, at two different time instances. The interface position is markedly different for the three cavity shapes at the inlet location, between the two time

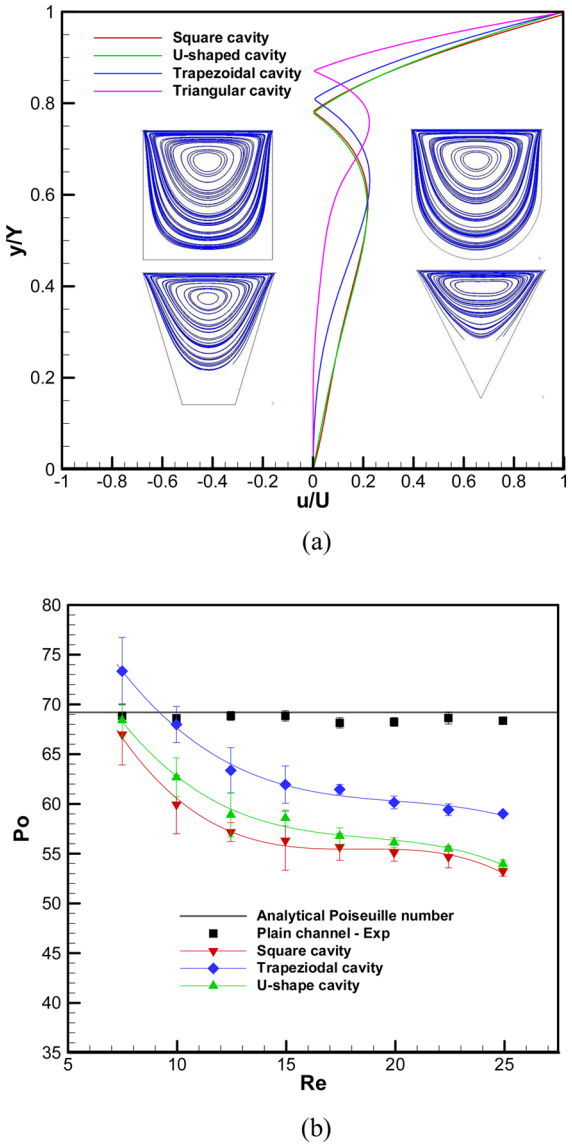

Figure 7. (a) Horizontal velocity variation versus height along the centerline of different cavities for Re = 1. The streamline patterns for the various cavity shapes are shown in the insets. (b) Variation of the Poiseuille number with Reynolds number for square, trapezoidal, and U-shaped cavities.

instances considered (Figure 8a). The difference persists at the mid location (Figure 8b) but vanishes at the outlet location (Figure 8c). The interface position for the three cavity shapes is approximately the same at $t = 0$ in Figure 8a. However, at $t = 10$ min, the interface has moved almost fully inside the square cavity, while the movement into the cavity is incomplete for the U-shaped cavity (Figure 8a). In contrast, the interface position does not change significantly over the 10 min experiment duration for the trapezoidal cavity (Figure 8a). At the mid location, square and U-shaped cavities exhibit a concave interface, whereas a clear convex interface is observed for trapezoidal cavities (Figure 8b). As explained above, the convex interface generated by a trapezoidal cavity is due to a force exerted by the vortex, being closer to the liquid–gas interface (see Figure 8d). These observations therefore lend credence to the simulation results, which also suggested that the vortex in a trapezoidal cavity resists the movement of the air–water

DOI: 10.1021/acs.langmuir.5b03666
Langmuir 2015, 31, 13373–13384

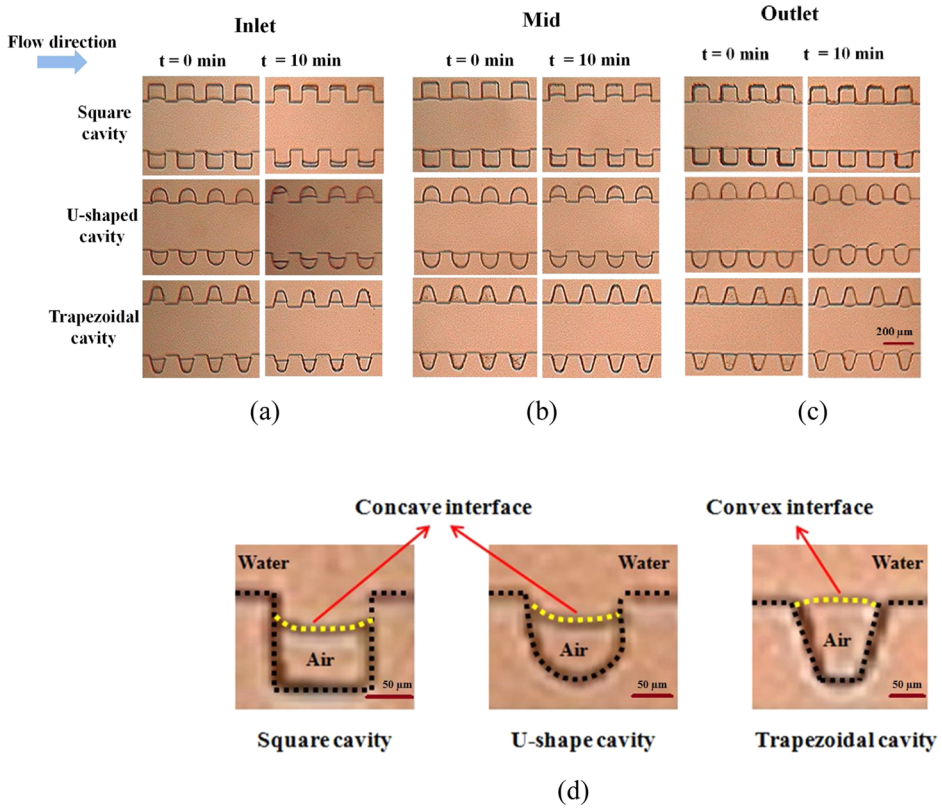

Figure 8. Visualization of air−water interface for square, U-shaped, and trapezoidal cavities: (a) at inlet, (b) mid section, and (c) outlet positions of the microchannel. The results are presented at two different time instances for Re = 10. (d) Enlarged view of the interface shape (concave and convex) at the channel middle section for square, U-shaped, and trapezoidal cavities. The air−water interface is marked by a yellow dotted line.

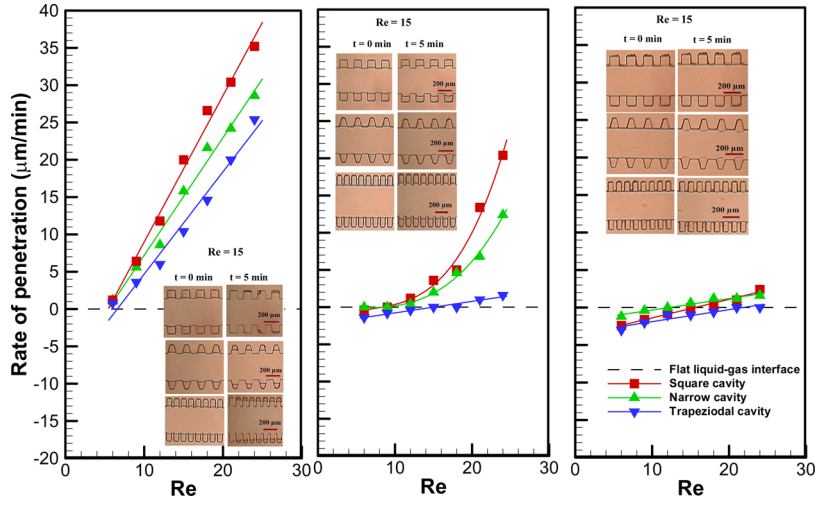

Figure 9. Rate of penetration of air−water interface for square, trapezoidal, and narrow rectangular cavities at all flow rates investigated. A baseline indicating flat liquid−gas interface also shown.

interface into the cavity, by applying a larger force on the interface.

To evaluate the importance of cavity shape and size on sustaining the trapped air over a period of time, the penetration rate of the air−water interface inside the cavity is evaluated. Each measurement is carried out over a 10 min period at a particular flow rate with images taken at 1 min intervals. At each section, i.e., inlet, mid and outlet regions, a total of 15 cavities were considered, and the penetration depth was averaged over all these cavities. Figure 9 depicts the variation of penetration rate of the air−water interface inside/outside the cavity for square, trapezoidal, and narrow rectangular cavities. Positive penetration rates indicate movement of the air−water meniscus inside the cavity, while negative rates indicate protrusion of the interface into the flow. An almost linear variation of penetration rate is observed for all the cavities under consideration at the inlet. It is also apparent that the penetration rate at the inlet is greater compared to the mid and outlet sections due to higher hydraulic pressure above the cavities. At the midsection, a rapid increase with Re is observed for square and narrow rectangular

DOI: 10.1021/acs.langmuir.5b03666
Langmuir 2015, 31, 13373−13384

cavities, while a linear variation is still observed for trapezoidal cavities. This exponential-type variation in the case of vertical wall geometries (square and narrow rectangular) reveals the rapid disappearance of air pockets at high flow rates.

If the structures have slightly inclined walls, the gap between the structures reduces along the length of the wall. Thus, the downward propagation of the liquid–gas meniscus experiences higher resistance due to increased in gas pressure in the inclined wall cavity compared to that for vertical wall cavity. It was experimentally observed by Forsberg et al.[9] that pillars with inclined walls are less prone to early collapse of CBS in *static* conditions. Our observation is therefore in agreement with the earlier finding, albeit under dynamic conditions. In a similar manner, increase in air pressure due to movement of the air–water interface inside a cavity resists the vanishing of air pockets; thus, a linear variation of penetration rate is observed for inclined wall geometries (trapezoidal). The role of pressure appears stronger than the role of vortex in delaying the wetting transition once the air–water interface progresses into the cavity.

6. DISCUSSION

Unlike static conditions, for positive flow rates, the dynamics of air in a cavity plays a crucial role in determining the interface position. At low flow rates, the pressure difference across a liquid–gas interface is not sufficiently large to force the interface into the cavity. In those situations, the dominance of hydrophobic characteristics of PDMS together with surface tension makes the interface convex in shape (Figure 10). However, at higher flow rates the hydraulic pressure and vortex dynamics cause the interface to assume a concave shape.

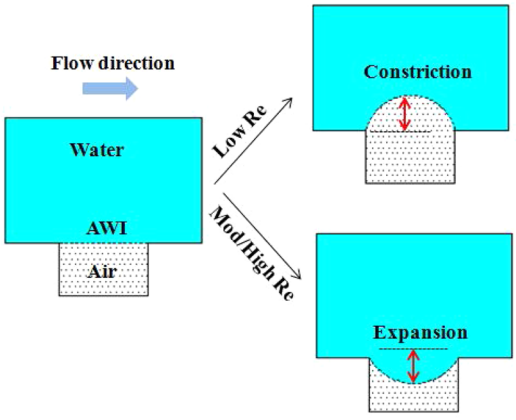

Figure 10. Flow regimes based on flow rates.

Earlier theoretical studies[41,42] assumed the liquid–gas interface to be flat and imposed a shear-free boundary condition there. However, discrepancies were observed between theoretical and experimental results, which were attributed to the deformation of the interface.[43] The deformation of the interface was substantiated by confocal microscopy-based measurements at discrete locations.[43,44] In most of the experimental studies,[29,43−46] structures were fabricated on the bottom wall making visualization difficult; therefore, information on the location and movement of the interface was incomplete. This crippled the ability to gain understanding of the interface dynamics and the effect of streamwise pressure changes on deformation of the interface. This aspect has been dealt with successfully in the present study by fabricating cavities on the side walls of the microchannel.

Some theoretical studies[47,48] have suggested that increase in the slip length is possible by suitably altering the interface shape (i.e., from concave to convex). However, our experiments show that the pressure drop is larger for convex-shaped interfaces (Figures 6a,c,d). The protrusion of the interface into the channel decreases the effective flow width (Figure 6b) causing constriction of the flow, thus increasing the pressure drop across the microchannel. Our results indicate that the gain caused by slip at the air–water interface is more than compensated by the loss created by constriction of the flow passage. This result is also supported by recent micro-PIV based measurements of Kwon et al.[49] Their results indeed show the presence of finite slip on convex air bubbles; however, an increase in overall pressure drop across the microchannel was observed with an increase in the bubble height. On the basis of this evidence, we propose that the increased constriction plays a more important role than increased slip at the interface, at least for flows at the microscale.

At higher flow rates, the air–water interface deforms into the cavity and assumes a concave shape (Figure 10). Therefore, the gain caused by slip at the air–water interface, the loss created by expansion of the flow into the cavity (leading to an deceleration/acceleration loss), and the gain caused by an increase in the flow width all become relevant. Bolognesi et al.[50] argued that the increase in flow throughput rate is due to increase in area of the microchannel by expansion of interface into the cavity. Similar views were put forward by Schonecker et al.,[51] that surface indentations reduce the effective radius of a bluff body, thereby leading to a reduction in drag force. Figure 4a shows that there is no net gain at Re = 7.5; however, the gain sets in at higher Reynolds number and continues up to the maximum value of Re investigated. Figure 4a also shows that the pressure drop in the Wenzel state is lower than in the Cassie–Baxter state for a given flow rate. This indicates that the increase in flow area has a tremendous impact on the pressure drop in a microchannel.

Another pertinent question is on the appropriateness of the shear-free boundary assumption (infinite slip length) at the liquid–gas interface. This assumption arises from the magnitude of the ratio of viscosities for a typical air–water system. This idealization leads to analytical predictions of effective slip length[2] higher than observed in experiments.[43] Few recent studies attributed this deviation to the liquid–gas interface curvature and local variation of slip length along the liquid–gas interface.[52,53] Hence, the underlying gas renders a finite resistance to the liquid flow. Kim et al.[54] argued that the air–water interface in effect resembles a no-slip boundary condition rather than a shear-free interface, based on numerical simulation results. On the contrary, micro-PIV based measurements of Byun et al.[55] revealed the existence of finite slip on the air–water interface under similar experimental conditions. Zheng et al.[56] ascribed the increase in interfacial stresses to the channel dimensions being less than the capillary length. Our measurements do not yield information about the no-slip boundary conditions on the interface, but the results suggest that the increase in the effective flow area is the main reason behind the reduction in pressure drop across structured microchannels.

DOI: 10.1021/acs.langmuir.5b03666
Langmuir 2015, 31, 13373−13384

7. CONCLUSIONS

In the present work, we have experimentally investigated the effect of size and shape of air cavities in delaying the Cassie−Wenzel transition. We have carried out experiments at flow rates corresponding to Re = 5−25 with cavities inserted into the side walls of a PDMS-based microchannel for easy visualization of the air−water interface dynamics. At low flow rates, the air−water interface of square cavities is found to protrude into the main channel flow, which causes an increase in pressure drop with time. However, significant growth of the air−water interface is not observed for another shape (narrow rectangular cavities) even though the gas fraction is the same in both cases. Comparison of the frictional resistance for Cassie and Wenzel states revealed that the latter one exhibits lower frictional resistance than the former. This is attributed to an increase in the flow width caused by complete filling of cavities by the liquid. The frictional resistance of narrow rectangular cavities is observed to be greater compared to square cavities, indicating that the former shape sustains air pockets over longer periods of time.

We propose that liquid-driven vortices in air cavities dissipate additional energy thereby delaying the CBS−WS transition. The numerical simulation further exposes the importance of these vortices. Out of the four cavity shapes considered in the study, vortices in the case of triangular cavities are observed to move closer to the air−water interface followed by trapezoidal, square, and U-shaped cavities. Experimental verification of the effect of liquid driven vortices on the air−water interface revealed that inclined-wall trapezoidal cavities delay the CBS−WS transition compared to square and U-shaped cavities. The penetration rate of the air−water interface follows a linear trend at the inlet of the microchannel for square, narrow rectangular, and trapezoidal cavity shapes. Exponential-type variation of penetration of the air−water interface for vertical wall cavities indicates rapid disappearance of air pockets at high flow rates for these cases compared to the inclined walls of trapezoidal cavities. One of the possible outcomes of the observed vortex-based tailoring of the liquid−gas interface is that the optimal meniscus position could be maintained throughout the microchannel by judicious choice of cavity shape along the length of the microchannel. We believe that these results are significant because not many ways to delay transition using a passive approach are currently known.

AUTHOR INFORMATION

Corresponding Author

*E-mail amit.agrawal@iitb.ac.in (A.A.).

Notes

The authors declare no competing financial interest.

ACKNOWLEDGMENTS

We are grateful to CEN (Center for Excellence in Nanotechnology), IIT Bombay, for providing access to the microfabrication facility for fabrication of microchannels. We are grateful to ISRO for supplying the funding to carry out this work.

REFERENCES

(1) Haeberle, S.; Zengerle, R. Microfluidic platforms for lab-on-a-chip applications. *Lab Chip* **2007**, *7*, 1094−1110.
(2) Lauga, E.; Stone, H. A. Effective slip in pressure-driven stokes flow. *J. Fluid Mech.* **2003**, *489*, 55−77.
(3) Wang, W.; Jones, T. B. Moving droplets between closed and open microfluidic systems. *Lab Chip* **2015**, *15*, 2201.
(4) Mats, L.; Young, R.; Gibson, G. T. T.; Oleschuk, R. D. Magnetic droplet actuation on natural (Colocasia leaf) and fluorinated silica nanoparticle superhydrophobic surfaces. *Sens. Actuators, B* **2015**, *220*, 5−12.
(5) Tsougeni, K.; Papageorgiou, D.; Tserepi, A.; Gogolides, E. "Smart" polymeric microfluidics fabricated by plasma processing: controlled wetting, capillary filling and hydrophobic valving. *Lab Chip* **2010**, *10*, 462−469.
(6) Wu, T.; Suzuki, Y. Engineering super hydrophobic surfaces as the microfluidic platform for droplet manipulation. *Lab Chip* **2011**, *11*, 3121.
(7) Liu, T.; Kim, C. J. Turning a surface super-repellent even to completely wetting liquids. *Science* **2014**, *346*, 1096−1100.
(8) Lauga, E.; Brenner, M. P.; Stone, H. A. In *Handbook of Experimental Fluid Dynamics*; Springer: New York, 2007; Chapter 19, pp 1219−1240.
(9) Forsberg, P.; Nikolajeff, F.; Karlsson, M. Cassie−Wenzel and Wenzel−Cassie transitions on immersed superhydrophobic surfaces under hydrostatic pressure. *Soft Matter* **2011**, *7*, 104.
(10) Huang, C. J.; Fang, W. F.; Ke, M. S.; Chou, H. Y. E.; Yang, J. T. A biocompatible open-surface droplet manipulation platform for detection of multi-nucleotide polymorphism. *Lab Chip* **2014**, *14*, 2057−2062.
(11) Ghosh, A.; Ganguly, R.; Schutzius, T. M.; Megaridis, C. M. Wettability patterning for high-rate, pumpless fluid transport on open, non-planar microfluidic platforms. *Lab Chip* **2014**, *14*, 1538−1550.
(12) Asmolov, E. S.; Dubov, A. L.; Nizkaya, T. V.; Kuehne, A. J. C.; Vinogradova, O. I. Principles of transverse flow fractionation of microparticles in superhydrophobic channels. *Lab Chip* **2015**, *15*, 2835−2841.
(13) Yoshimitsu, Z.; Nakajima, A.; Watanabe, T.; Hashimoto, K. Effects of surface structure on the hydrophobicity and sliding behaviour of water droplets. *Langmuir* **2002**, *18*, 5818−22.
(14) Boreyko, J. B.; Chen, C. H. Restoring Superhydrophobicity of Lotus Leaves with Vibration-Induced Dewetting. *Phys. Rev. Lett.* **2009**, *103*, 174502.
(15) Lee, C.; Nam, Y.; Lastakowski, H.; Hur, J. I.; Shin, S.; Biance, A. L.; Pirat, C.; Kim, C. J.; Ybert, C. Two types of Cassie-to-Wenzel wetting transitions on superhydrophobic surfaces during drop impact. *Soft Matter* **2015**, *11*, 4592−4599.
(16) Whyman, G.; Bormashenko, E. Wetting Transitions on Rough Substrates: General Considerations. *J. Adhes. Sci. Technol.* **2012**, *26*, 207−220.
(17) Bormashenko, E.; Musin, A.; Whyman, G.; Zinigrad, M. Wetting Transitions and Depinning of the Triple Line. *Langmuir* **2012**, *28*, 3460−3464.
(18) Bobji, M. S.; Kumar, S. V.; Asthana, A.; Govardhan, R. N. Underwater Sustainability of the "Cassie" State of Wetting. *Langmuir* **2009**, *25* (20), 12120−12126.
(19) Poetes, R.; Holtzmann, K.; Franze, K.; Steiner, U. Metastable Underwater Superhydrophobicity. *Phys. Rev. Lett.* **2010**, *105*, 166104.
(20) Samaha, M. A.; Tafreshi, H. V.; Gad-el-Hak, M. Sustainability of superhydrophobicity under pressure. *Phys. Fluids* **2012**, *24*, 112103.
(21) Krupenkin, T. N.; Taylor, J. A.; Wang, E. N.; Kolodner, P.; Hodes, M.; Salamon, T. R. Reversible Wetting-Dewetting Transitions on Electrically Tunable Superhydrophobic Nanostructured Surfaces. *Langmuir* **2007**, *23*, 9128−9133.
(22) Lei, L.; Li, H.; Shi, J.; Chen, Y. Diffraction Patterns of a Water-Submerged Superhydrophobic Grating under Pressure. *Langmuir* **2010**, *26* (5), 3666−3669.
(23) Whyman, G.; Bormashenko, E. How to Make the Cassie Wetting State Stable? *Langmuir* **2011**, *27*, 8171−8176.
(24) Reyysat, M.; Yeomans, J. M.; Quere, D. Impalement of fakir droplets. *Europhys. Lett.* **2008**, *81*, 26006.
(25) Mall, A.; Agrawal, A.; Singh, R. K.; Joshi, S. S. Numerical characterization of laminar bulk flow over textured surfaces. *J. Micro-Nanolith MEM.* **2011**, *10* (023008), 1−11.

DOI: 10.1021/acs.langmuir.5b03666
Langmuir 2015, 31, 13373−13384

(26) Xue, Y.; Chu, S.; Lv, P.; Duan, H. Importance of hierarchical structures in wetting stability on submersed superhydrophobic surfaces. *Langmuir* **2012**, *28*, 9440−9450.
(27) Hensel, R.; Finn, A.; Helbig, R.; Killge, S.; Braun, H. G. In Situ Experiments To Reveal the Role of Surface Feature Sidewalls in the Cassie−Wenzel Transition. *Langmuir* **2014**, *30*, 15162−15170.
(28) Samaha, M. A.; Tafreshi, H. V.; Gad-el-Hak, M. Superhydrophobic surfaces: From the lotus leaf to the submarine. *C. R. Mec.* **2012**, *340*, 18−34.
(29) Dey, R.; Raj, K.; Bhandaru, N.; Mukherjee, R.; Chakraborty, S. Tunable hydrodynamic characteristics in micro-channels with biomimetic superhydrophobic (lotus leaf replica) walls. *Soft Matter* **2014**, *10*, 3451−3462.
(30) de Oliveira, L. R.; Lopes, D. M.; Ramos, S. M. M.; Mombach, J. C. M. Two-dimensional modeling of the superhydrophobic behavior of a liquid droplet sliding down a ramp of pillars. *Soft Matter* **2011**, *7*, 3763.
(31) Biben, T.; Joly, L. Wetting on Nanorough Surfaces. *Phys. Rev. Lett.* **2008**, *100*, 186103.
(32) Lee, C.; Kim, C. J. Influence of surface hierarchy of superhydrophobic surfaces on liquid slip. *Langmuir* **2011**, *27*, 4243−4248.
(33) Carlborg, C. F.; van der Wijngaart, W. Sustained superhydrophobic friction reduction at high liquid pressures and large flows. *Langmuir* **2011**, *27* (1), 487−493.
(34) Bormashenko, E. Progress in understanding wetting transitions on rough surfaces. *Adv. Colloid Interface Sci.* **2015**, *222*, 92−103.
(35) Lv, P.; Xue, Y.; Shi, Y.; Lin, H.; Duan, H. Metastable States and Wetting Transition of Submerged Superhydrophobic Structures. *Phys. Rev. Lett.* **2014**, *112*, 196101.
(36) Luo, C.; Xiang, M.; Heng, X. A stable intermediate wetting state after a water drop contacts the bottom of a microchannel or is placed on a single corner. *Langmuir* **2012**, *28*, 9554−9561.
(37) del Campo, A.; Greiner, C. SU-8: a photoresist for high-aspect-ratio and 3D submicron lithography. *J. Micromech. Microeng.* **2007**, *17*, R81−R95.
(38) Davies, J.; Maynes, D.; Webb, B. W.; Woolford, B. Laminar flow in a microchannel with superhydrophobic walls exhibiting transverse ridges. *Phys. Fluids* **2006**, *18*, 087110.
(39) Chakraborty, S.; Anand, K. D. Implications of hydrophobic interactions and consequent apparent slip phenomenon on the entrance region transport of liquids through microchannels. *Phys. Fluids* **2008**, *20*, 043602.
(40) Zhang, T.; Shi, B.; Chai, Z. Lattice Boltzmann simulation of lid-driven flow in trapezoidal cavities. *Comput. Fluids* **2010**, *39*, 1977−1989.
(41) Philip, J. R. Flows Satisfying Mixed No-Slip and No-Shear Conditions. *Angew. Math. Phys.* **1972**, *23*, 353−372.
(42) Lauga, E.; Stone, H. A. Effective slip in pressure-driven stokes flow. *J. Fluid Mech.* **2003**, *489*, 55−77.
(43) Tsai, P.; Peters, A. M.; Pirat, C.; Wessling, M.; Lammertink, R. G. H.; Lohse, D. Quantifying effective slip length over micro-patterned hydrophobic surfaces. *Phys. Fluids* **2009**, *21*, 112002.
(44) Ou, J.; Rothstein, J. P. Direct velocity measurements of the flow past drag-reducing ultrahydrophobic surfaces. *Phys. Fluids* **2005**, *17*, 103606.
(45) Ou, J.; Perot, B.; Rothstein, J. P. Laminar drag reduction in microchannels using ultrahydrophobic surfaces. *Phys. Fluids* **2004**, *16*, 4635.
(46) Lee, A.; Kim, H. Y. Does liquid slippage within a rough channel always increase the flow rate? *Phys. Fluids* **2014**, *26*, 072002.
(47) Davis, A. M. J.; Lauga, E. Geometric transition in friction for flow over a bubble mattress. *Phys. Fluids* **2009**, *21*, 011701.
(48) Teo, C. J.; Khoo, B. C. Flow past superhydrophobic surfaces containing longitudinal grooves: effects of interface curvature. *Microfluid. Nanofluid.* **2010**, *9*, 499−511.
(49) Kwon, B. H.; Kim, H. H.; Jeon, H. J.; Kim, M. C.; Lee, I.; Chun, S.; Go, J. S. Experimental study on the reduction of skin frictional drag in pipe flow by using convex air bubbles. *Exp. Fluids* **2014**, *55*, 1722.
(50) Bolognesi, G.; Cottin-Bizonne, C.; Pirat, C. Experimental evidence of slippage breakdown for a superhydrophobic surface in a microfluidic device. *Phys. Fluids* **2014**, *26*, 082004.
(51) Schönecker, C.; Hardt, S. Assessment of drag reduction at slippery, topographically structured surfaces. *Microfluid. Nanofluid.* **2015**, *19*, 199.
(52) Schönecker, C.; Baier, T.; Hardt, S. Influence of the enclosed fluid on the flow over a micro-structured surface in the Cassie state. *J. Fluid Mech.* **2014**, *740*, 168−195.
(53) Gaddam, A.; Garg, M.; Agrawal, A.; Joshi, S. S. Modeling of liquid-gas meniscus for textured surfaces: Effect of curvature and local slip length. *J. Micromech. Microeng.* **2015**, *25*, 125002.
(54) Kim, T. J.; Hidrovo, C. Pressure and partial wetting effects on superhydrophobic friction reduction in microchannel flow. *Phys. Fluids* **2012**, *24*, 112003.
(55) Byun, D.; Kim, J.; Ko, H. S.; Park, H. C. Direct measurement of slip flows in superhydrophobic microchannels with transverse grooves. *Phys. Fluids* **2008**, *20*, 113601.
(56) Zheng, W.; Wang, L. P.; Or, D.; Lazouskaya, V.; Jin, Y. Role of Mixed Boundaries on Flow in Open Capillary Channels with Curved Air − Water Interfaces. *Langmuir* **2012**, *28*, 12753−12761.

DOI: 10.1021/acs.langmuir.5b03666
Langmuir 2015, 31, 13373−13384